International Journal of Hydrogen Energy 164 (2025) 150764

Contents lists available at ScienceDirect

International Journal of Hydrogen Energy

journal homepage: www.elsevier.com/locate/he

High temperature tensile strength of ultrathin 3YSZ tapes: An experimental study combining Weibull theory and fracture mechanics

Ilaria Bombarda [a,*], Felix Wich [a], Nico Langhof [a], Carolin Sitzmann [a,b], Stefan Schafföner [a]

[a] Chair of Ceramic Materials Engineering (CME), University of Bayreuth, Prof.-Rüdiger-Bormann-Str. 1, 95447, Bayreuth, Germany
[b] Fraunhofer ISC, Center for High Temperature Materials and Design HTL, Gottlieb-Keim-Strasse 62, 95448, Bayreuth, Germany

ARTICLE INFO

Keywords:
3YSZ
Tensile
SOC
High temperature
Ultrathin

ABSTRACT

High temperature electrolysis (HTEL) has several advantages compared to other types of solid oxide cell (SOC) technologies, including an increased efficiency at high temperature when combined with an exothermic process. To reduce costs, increase lifetime and improve scale up production of electrolyte supported SOCs, an important property is the mechanical stability of the cell, which is provided by the ceramic electrolyte. In this work, the tensile mechanical properties of ultrathin (t = 90 μm) 3% yttria-stabilized zirconia electrolytes were measured at room and operating temperature (T = 850 °C). In-situ nanoindentation was also performed to study the 3YSZ local mechanical properties at room and high temperature. The calculated characteristic tensile strength and Weibull modulus allowed the evaluation of mechanical properties with improved reliability compared to the previously reported values in the literature, deriving from the substantially larger tested material volume. An extensive fracture analysis revealed porosity or particle inclusions at the fracture origin. The defect size and strength relation showed a deviation from linear elastic fracture mechanics, identifying the presence of subcritical crack growth.

1. Introduction

In the pursuit of carbon neutrality by 2050, hydrogen production via water electrolysis is a fast growing market. Together with electrification, it represents a key technology for decarbonization, with a world goal electrolysis capacity of 230 GW by 2030. [1–5]. High temperature electrolysis (HTEL) is a very promising technology to produce green hydrogen [6] at about T = 850 °C as it has a higher efficiency compared to the state-of-the-art low temperature electrolysis technologies [7,8]. Some important technological and economical challenges are, however, hindering HTEL from expanding the electrolysis capacity, namely long-term stability, degradation [9] and material costs [2]. Fundamental research on the materials is therefore determining the cost-efficiency of solid oxide cells (SOCs) [6,10,11].

Compared to electrode-supported cells, electrolyte-supported cells (ESCs) are more robust and have the ability to withstand thermal cycling. These qualities can extend the stack lifetime compared to electrode-supported cells and are more relevant than the maximum power density [7]. On the other hand, ESCs material costs are more than 50 % higher compared to electrode-supported SOCs when scandia-stabilized zirconia (SSZ) electrolytes are implemented [2]. As SOCs material costs are contributing to more than 29 % of the stack costs [2], it is easy to understand how important material research is for efficiency. A correct dimensioning of parts based on reliable strength values is also essential to minimize material waste.

For ESCs, the electrolyte is the load bearing component, and the overall mechanical strength relies on it. To improve the cells' performance, it is desirable to reduce the electrolyte thickness, as the total ohmic losses are proportional to the resistance ionic sheet of the electrolyte [12]. Mechanical evaluation of cearmic thin tapes and thin multi-layer components such as electrolytes and SOCs is technically challenging due to the problematic machining and the high material flexibility. To overcome the problem of inefficient machining, which would invalidate a standard bending or tensile test ending up in an evaluation of the machining and not of the materials itself, ring-on-ring (RoR), ball-on-three-balls (B3B) or similar tests are generally implemented [13–31]. However, especially for ultrathin tapes (t < 60 μm), these tests are not able to evaluate a significant and representative effective volume, leading to an overestimation of the material strength [15,19,25]. With the aim of testing a significant effective volume, a method to test thin tapes (t = 90 μm) in tensile was previously

---

* Corresponding author.
E-mail addresses: ilaria.bombarda@uni-bayreuth.de (I. Bombarda), felix.wich@uni-bayreuth.de (F. Wich), nico.langhof@uni-bayreuth.de (N. Langhof), carolin.sitzmann@isc.fraunhofer.de (C. Sitzmann), stefan.schaffoener@uni-bayreuth.de (S. Schafföner).

https://doi.org/10.1016/j.ijhydene.2025.150764
Received 14 May 2025; Received in revised form 18 July 2025; Accepted 29 July 2025

developed by the authors [32]. The same testing setup was adapted in this work to allow the evaluation of tensile mechanical properties of ultrathin (t = 90 μm) 3 mol % yttria stabilized zirconia (3YSZ) tapes at operating temperature (T = 850 °C). The mechanical properties at room temperature with the same effective volume were then also determined as means of comparison and, for the room as well as for the high temperature tests, a statistically relevant number of samples (n = 30) was assessed. In order to measure the local mechanical properties of the electrolyte at high temperature, in-situ nanoindentation was performed on 3YSZ tapes.

The material properties of monolithic ceramic materials are strongly related with the defect size and distribution [33–37]. For this reason, a fracture surface analysis was attempted to determine the critical defect size for high as well as for room temperature tests. With the aim of linking the strength to the defect size, the fractographical analysis was performed on every sample. The extensive fractographic analysis allowed the identification of the crack-inducing defects for almost all of the valid samples. All of the measured defects were classified based on the size, nature and position [38–41]. The comparison of the fractographic analysis between room and high temperature tests delineated the conformity of the defect size between the two categories and an important difference in the defect positions. It was finally possible to correlate the strength with the defect size for at least 24 samples for each tested temperature. Most of the defects were evaluated as sub-critical, denoting the presence of sub-critical crack growth. Only a few defects were considered critical, as the relation between strength and measured defect size followed the linear elastic fracture mechanics (LEFM) theory.

2. Materials and methods

2.1. Mechanical characterization

The 3YSZ foils (90 μm nominal thickness) were produced via tape casting, sintered (T = 1400 – 1500 °C) and laser cut by the company Kerafol (KERAFOL Keramische Folien GmbH, Germany) [42], whereas all of the material belonged to the same production batch. The material was analyzed via X-ray diffraction (XRD) using CuKα radiation (D8 Discovery A25, Bruker GmbH, Germany) and Rietveld analysis was performed to determine the phase composition (TOPAS software, Bruker GmbH, Germany). The tensile sample geometry was chosen based on previous studies [20,43–45], with a sample length of 50 mm and 160 mm respectively for the room and high temperature tests. The sample preparation was based on the authors' past work [32]. The first step after the sample lasering was the grinding of the sample edges with a 5-axis grinding machine (Ultrasonic 20 Sauer DMG Mori GmbH, Germany) using a grinding 2 mm diameter diamond tool (Schott Diamantwerkzeuge GmbH, Germany, D25 FEPA diamond grain size). The multistep wet grinding was performed on samples with 4 mm width up until the reaching of the width of 2.5 mm. The tool rotation was 24000 rot/min, the tool velocity was 400 mm/min, resulting in 0.1 mm material removed for each step, which was repeated four times for each sample. Fig. 1a shows the final sample geometry, with the ground edges marked in yellow. The smaller width compared with our previous work was chosen to reduce the risk of invalid failure corresponding to the maximum temperature gradient, which was located in a laser cut edge for the high temperature sample geometry.

A custom made setup was implemented for the tensile testing, as described in detail in our previous work [32], with the help of a swivel head (GAL8-UK, Scheffler GmbH, Germany) to minimize misalignment [46,47]. Steel cap stripes and pins were glued to the samples with the help of a steel reinforced epoxy resin glue (JB Weld, USA), for a moment-free coupling with the tensile test setup. The tests were performed with a high temperature universal testing machine (Z050 TEW ZwickRoell Testing Systems GmbH, Austria) and a 5 kN load cell. The sample deformation was recorded with a laser extensometer with 1 μm precision (laserXtens 7–220 HP, ZwickRoell Testing Systems GmbH, Austria). For the high temperature tests, a cold gripping concept was realized, as shown in Fig. 1b, utilizing the same grips used with the room temperature test. The hot area was about 100 mm in height, and the sample length (160 mm) was sufficient to prevent the glue at the gripping to start degrading due to heat. The room temperature tensile tests were performed at T = 23 °C and 51 % relative humidity, with a F = 10 N preload and a test velocity of v = 1 mm/min. The high temperature tensile tests procedure was the following: application of a F = 10 N preload, heating up phase until T = 850 °C (heating rate 25 °C/min), holding of the goal temperature for t = 5 min, testing until failure with a test velocity of v = 1 mm/min, cooling down. Thanks to two thermocouples (Fig. 1b) in the sample vicinity, the testing temperature was determined with a good precision (± 5 °C). A sample size of 30 for each temperature was chosen for a total amount of 60 tested samples. The samples which did not fail in the smaller cross-sectional area were excluded and considered as invalid [43]. In order to carry out the microstructural analysis of the crack initiation, the room temperature tests were carried out with a scotch tape (Tesa SA, Switzerland) glued on one side of the sample. The obtained data were analyzed with one-way analysis of variance (ANOVA).

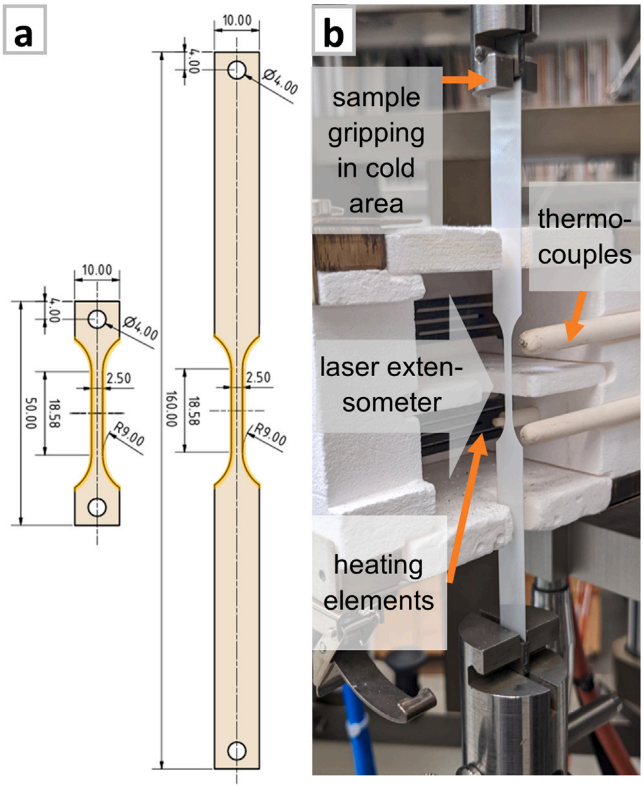

Fig. 1. (a) Sample geometry after grinding for the room temperature (left) and high temperature (right) tensile test; the yellow line indicates the edges which were ground; (b) High temperature tensile test setup with cold gripping system including the thermocouples for local temperature recording and the laser-extensometer for deformation measurements. (For interpretation of the references to color in this figure legend, the reader is referred to the web version of this article.)

2.2. Microstructural characterization

The microstructure was analyzed with a scanning electron microscope (SEM) (Sigma 300 VPB, Zeiss, Germany) with a backscattered electron detector, moreover an energy dispersive X-ray analysis (EDX) was performed. Before the analysis, all the samples were cleaned with the help of an ultrasonic bath and burned with a gas burner. For

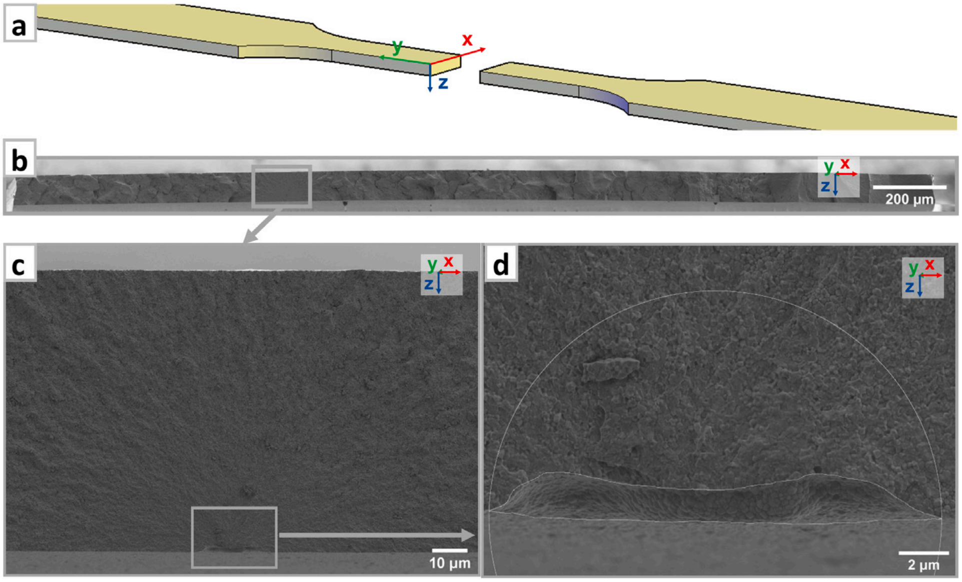

Fig. 2. (a) Schematic view of a sample after the high temperature test. The y axis was the direction of load application and the xz axis indicated the fracture plane; (b) SEM overview of the whole crack surface of a sample after the test at room temperature. Here it was possible to identify the crack initiation point due to the presence of hackle lines; (c) magnification of the crack initiation point for a near-surface defect where the crack Hackle lines can be identified; (d) further enlargement of the defect. The two white profiles traced are corresponding to the defect perimeter and to the semicircle that includes the complete defect and has the diameter on the sample surface.

each valid test (n = 27 for high temperature and n = 27 for room temperature), the two broken pieces were analyzed and the location of crack initiation was identified in almost every sample [38,48,49]. In total, 108 crack surfaces were analyzed, and the extensive analysis allowed the identification of the crack initiation point for all the 27 room temperature samples and for 24 out of 27 high temperature samples. In Fig. 2 it is shown how the crack surface was analyzed and the critical defects observed. The defects, which consisted in porosity or particle inclusions, were measured using the software ImageJ (National Institutes of Health, USA). The defects dimensions were characterized by measuring the Feret maximum diameter [50] and the diameter for semi-circular surface defects and circular bulk defects [39]. For each particle inclusion defect, EDX was performed to characterize the particle chemistry. The material grain size was determined with the linear intercept procedure [51,52] using the software ImageJ on an area of about 80 μm^2. The micrographs were realized at the SEM with a backscattered electrons detector after embedding (Technovit 5071, Kulzer GmbH, Germany), grinding and polishing with SiC paper (Tegramin, Struers Struers ApS, Denmark), de-embedding and thermal etching (T = 1250 °C, 1 h).

2.3. In-situ nanoindentation

Nanoindentation was performed with an in-situ picoindenter (Hysitron PI 89 SEM PicoIndenter, Bruker, USA) in the scanning electron microscope (SEM), using a cubic boron nitride (cBN) indenter tip in Berkovich geometry. The tests were carried out at room temperature and high temperature: T = 250, 450, 650 °C and 850 °C. Due to technical reasons, the test at T = 850 °C was considered invalid. The sample, which consisted of a rectangular (size about 4×3 mm^2) laser-cut 3YSZ tape, was clamped to the stage with a Al_2O_3 disc (diameter 6 mm) between the sample and the stage. In this way, the machine compliance was minimized and it was possible to test the as-fired sample surface. For each temperature, a series of 10 cyclic indents was performed. Before each series of indents, a temperature calibration was executed, making sure that the indentation tip and sample temperature were constant. Each cyclic indent test consisted of 20 steps of loading and unloading with increasing force until the maximum of 250 mN was reached. The values of hardness and Young's modulus were calculated based on the method of Oliver and Pharr [53].

3. Results and discussion

3.1. Mechanical characterization

The mechanical tests at room and high temperature resulted in an excellent (90 %) validity rate, with 27 valid samples out of 30 total samples tested. All of the samples after the test are shown in Fig. 3. To prevent the sample breaking in multiple pieces, in order to allow the localization of the crack initiation point, a tape was glued on the room temperature samples on one side. However, the high temperature tested samples did not break in many pieces. Therefore it was possible to find the sample fragments for the fractographical analysis for 24 out of 27 samples without the tape application. The difference in amount of broken pieces comes from the discrepancy of energy released after the crack, which is higher at room temperature. To consistently compare the high and room temperature strength, samples from the same batch were chosen, and the sample geometry was designed to obtain the same effective volume tested V_{eff}. The values of thickness, width and sample volume are reported in Table 1. In the table, the room temperature tensile test data from our previous work is included for means of comparison [32], where samples had a slightly higher width. The mechanical properties in terms of characteristic strength, mean strength, median strength, Weibull modulus and Young's modulus for the three groups of data are outlined in Table 1. The characteristic strength is the strength corresponding to the probability of failure $p \approx 63.2$ % [36]. The Weibull plots are depicted in Fig. 4.

As it can observes from the results, the characteristic strength at T = 850 °C was about 50 % lower compared to the strength at room temperature. The strength values and differences between room and T = 850 °C were comparable with previous studies [19,54], which reported a difference of 43%. It is very important to specify that the type of test can affect the strength estimation. In particular the bending tests are conceived to have the maximum stress concentrated at the sample surface. Therefore the mechanical bending properties are largely influenced by the sample surface quality. Tensile testing is an evaluation of the whole sample volume. As it is plausible that the bulk defect distribution varies from the surface, the mechanical properties can then vary consistently. The Young's modulus was higher for room temperature compared to high temperature tests, which is in

Table 1
Mechanical properties of the 3YSZ samples tested at room and high temperature. For thickness, width, effective volume (V_{eff}) and Young's modulus (E) the mean and standard deviation are reported, while for the characteristic strength the 90% confidence interval is specified.

	Tested /valid samples	Thickness (mm)	Width (mm)	Characteristic strength σ_0 (MPa)	Mean strength (MPa)	Median strength (MPa)	Weibull modulus m	V_{eff} (mm^3)	E (GPa)
T = 25 °C	27/30	0.086 ± 0.03	2.55 ± 0.02	1174 (964|1251)	1129	1151	13.6	4.1 ± 0.2	198 ± 12
T = 25 °C[a]	30/33[a]	0.085 ± 0.03[a]	3.25 ± 0.07[a]	1104 (986|1202)[a]	1068[a]	1060[a]	14.2[a]	5.1 ± 0.2[a]	–
T = 850 °C	27/30	0.085 ± 0.03	2.55 ± 0.03	576 (507|600)	556	561	14.8	4.1 ± 0.1	170 ± 9

[a] Results from our previous work [32].

Fig. 3. Overview of the complete set of tested samples. On the top of the picture are positioned the 30 samples tested at room temperature and on the bottom the 30 samples tested at high temperature. The invalid samples are marked with an orange cross. (For interpretation of the references to color in this figure legend, the reader is referred to the web version of this article.)

agreement with previous studies [54]. The decrease of strength and Young's modulus from room to high temperature can be explained with different factors, one of which is the 3YSZ toughening transformation, which is temperature dependent. As for the sample analyzed, 3YSZ is in the tetragonal metastable phase, the mechanical stresses induce the phase transformation (tetragonal to monoclinic) leading to a local grain expansion and a crack closure. At medium temperatures (T = 450 °C), the toughening mechanism becomes less relevant as the energy for the tetragonal to monoclinic phase transformation is lower [55]. At T = 850 °C, the toughening mechanism is not relevant as the tetragonal phase is stable [56,57]. The lack of toughening mechanism, the absence of stable growth crack regime at T = 900 °C compared to room temperature [57] and the plasticity observed at higher temperatures [58] are the mechanisms which contributed to the lower mechanical properties observed at high temperature.

Concerning the difference between the two sets of results at room temperature, the ANOVA Tukey means test indicated a significant means difference at the $\alpha = 0{,}05$ level. This result states the statistical means difference between the two groups of strength data at room temperature, and it can be attributed to the tested volume difference, which is small but not negligible. The samples, which had a smaller volume tested resulted in having a higher average strength, which is in accordance with the Weibull theory. The Weibull plot for the room and high temperature tests is presented in Fig. 4. As it can be seen from the graph slopes and m values, the Weibull moduli did not differ relevantly. The Weibull modulus is, in theory, an expression of the flaw size and frequency, therefore this result could suggest that the critical defect distribution did not vary between the high and room temperature tests. However, this assumption was only partially confirmed with the fractographic analysis (see next paragraph). The characteristic strength was also plotted as a function of volume tested, and an estimation for the strength was calculated based on the Weibull theory given in the following equation [59]:

$$\sigma_1(R)^{\mathrm{m}} V_1 = \sigma_{\mathrm{x}}(R)^{\mathrm{m}} V_{\mathrm{x}} \tag{1}$$

where $\sigma_1(R)$ is the stress corresponding to the reliability R (in case of the characteristic stress R = 63.2%), V_1 is the effective volume tested, m is the Weibull modulus measured, and the right term of the equation corresponds to the stress with the same reliability, same Weibull modulus but different effective volume. The plot for the characteristic strength and for the 90 % reliability range is shown in Fig. 5. This plot is essential for the dimensioning of ceramic parts. Since the volume tested in tensile was higher than the one tested in B3B and RoR tests, it was still smaller compared to the complete size of cells in the stack. Considering a 100 × 150 mm^2 cell and a t = 90 μm thickness, the electrolyte volume is about 1350 mm^3, which is about 330 times the tested volume during tensile testing (Table 1). It was estimated that the 3YSZ electrolytes with the size of a complete cell size had a characteristic strength of $\sigma_{0,\ RT} \approx 700$ MPa and $\sigma_{0,\ 850\ °C} \approx 370$ MPa.

3.2. Fracture analysis

The analysis of the fracture surface after the test allowed the identification of the crack initiation point, as illustrated in Fig. 2. As it can observed from Fig. 2b, the crack initiation area was recognized due to the presence of a flat area, where thanks to a greater magnification (Fig. 2b, c) fracture hackle lines were visible. The hackle lines were described as lines on the surface running in the local direction of the cracking [38]. These lines pointed to the defect and end up in the so called fracture mirror, which was the flatter concentric semi-circular (or circular in the case of a bulk defect) area closest to the defect. These areas are not exactly definable for ceramics, but are usually clearly visible in the case of glass materials [38]. For this reason, a size evaluation of the mirror was not attempted even if this value can be useful for the evaluation of the crack propagation velocity. What was rather identified unmistakably is the defect size, which was outlined by a thin white line in Fig. 2c. The outlined circular perimeter was instead the semicircle which had the diameter on the sample surface that completely included the defect.

As mentioned in Section 2, a tape on one sample side allowed the fracture surface analysis, preventing the sample from breaking in many splinters due to the releases high energy accumulated before fracture. For the high temperature tests, this expedient was not needed, as the stress at which the samples broke was not high enough to fragment the samples in many pieces. Therefore the fractured surface was easily recognizable. The fractographic analysis distinguished a wide range of defect types: secondary particle inclusions, large porosity, porosity regions (regions with high density of small porosity), as well as surface defects. The nature of the defects did not differ substantially between room and high temperature tests. Thus, examples from both samples are depicted in Fig. 6, with the aim of clarifying at first how the defects were measured and classified. Some defects were found at the sample surface, others in the sample bulk. The defects were distinguished in

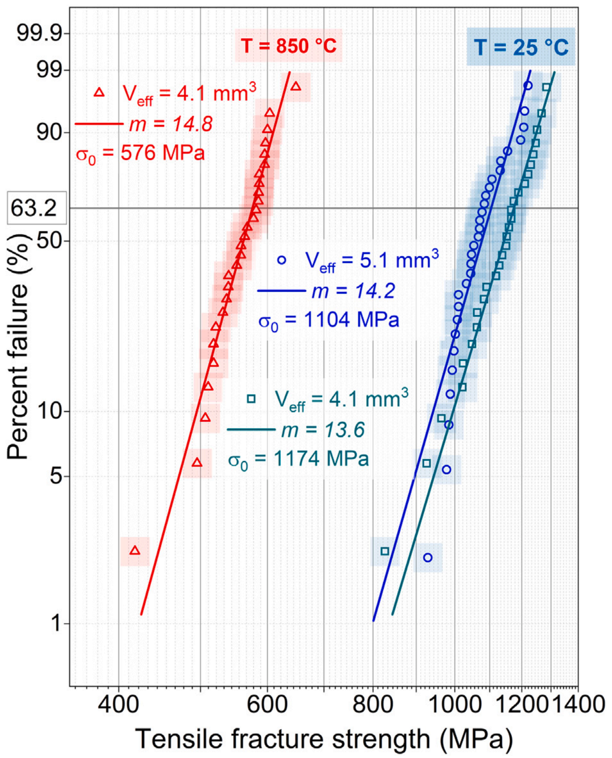

Fig. 4. Weibull plot of all the tensile tests performed at T = 25 °C and at T = 850 °C which are summarized in Table 1: the high temperature tests curve is on the left part of the graph, indicating a lower tensile strength, while the two sets of room temperature tests are on the right. A slight shifting of the room temperature tests with lower effective volume tested on the right is visible. The Weibull parameter *m* corresponds to the line pendence.

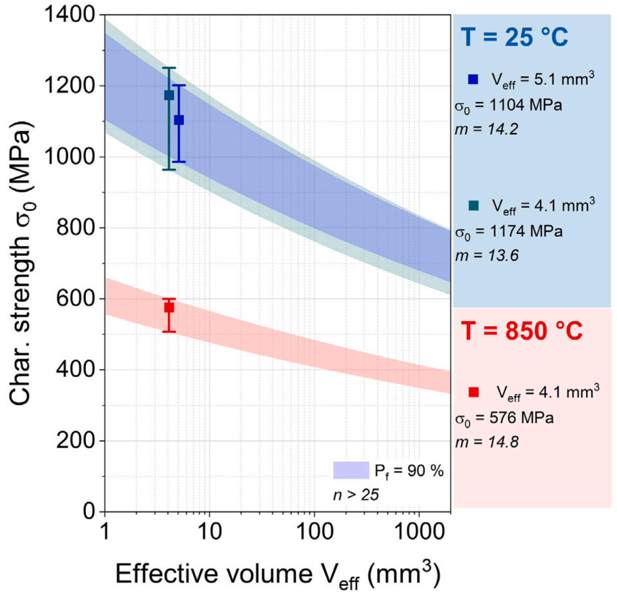

Fig. 5. The characteristic strength as a function of the effective volume is shown for the three sets of data, at room and high temperature; the bars indicate the 90 % interval, which was also calculated for higher effective volume utilizing Eq. (1).

two groups: near-surface defects (Figs. 2 and 6a) and bulk defects (Fig. 6b). The definition of a near-surface defect is, according to the literature, a particle where the distance from the sample surface is less than the maximum diameter. In order to classify these defects consistently, the maximum and minimum Feret diameters were measured for each defect, which are, respectively, the maximum and minimum calliper diameters measurable in a two-dimensional particle. In Fig. 6c, d, two bulk defects are shown, and the maximum Feret diameter (D_{Fmax}) and minimum Feret diameter (D_{Fmin}) are determined. They were measured after delineating the defect, as shown in the figures from the orange line. Thus, the definition of near-surface defect is the defect where $D_{Fmax} < D_{D\text{-}S}$, where $D_{D\text{-}S}$ is defined as the minimum distance from the defect to the sample surface, and it can be seen in Fig. 6b.

The particle inclusion defects were analyzed via EDX. Only two elements were found, which were aluminum and oxygen. It is very reasonable to presume that the particles were Al_2O_3 which was most likely an impurity from the production process. In Fig. 6e the fracture surface correspondent to a bulk particle inclusion defect is represented: the EDX analysis of the inclusion allowed the identification as Al_2O_3 particle, including the clearer round portions, which appear like melted parts. In Fig. 6f, an inclusion defect was observed, where the Al_2O_3 particle was not in its original place. The empty space left matched exactly the particle shape. Because of this important evidence, it was very difficult to state if, originally, a porosity defect did not have a particle inclusion in the cavity. This is the reason why in the further data interpretation, the difference between pore and inclusion defect was not taken into account. In Fig. 6g, a porosity defect in a high temperature test was magnified and it is clearly visible how the fractured surface differed from the pore area. Some of the grains were cleaved on the fractured surface, testifying a partial inter-granular fracture. As some entire grains are also present, the fracture micromechanism was described as mixed, meaning partly inter-granular and partly trans-granular. On Fig. 7, the fracture surface at higher magnification is shown for the room and the high temperature test. The room temperature sample showed a similar fracture surface conformation compared to the high temperature sample, where some grains were complete and some grains were cleaved. Yet a difference could be noticed, as at high temperature the amount of cleaved grains was lower than for the room temperature case. The difference was attributed to the increased atom mobility and decrease in boundary phase viscosity at high temperature. Both phenomena facilitate the inter-granular fracture at high temperature [38] and were the reasons for the lower strength and Young's modulus at high temperature.

A summary of the defects classification and measurement is reported in Table 2. A main difference between the room and high temperature fracture analysis was the defect location. For the high temperature tests, the crack starting defect was in the bulk material or at the near-surface, while for the room temperature tests all defects were found to be near-surface defects. The slight difference in defect size between room and high temperature (D_{Fmax} and area) can be associated to the defect location, as the surface defects are more critical [60,61]. As it will be explained later in this paragraph, the equivalent crack size parameter a_{eq} was calculated to compare surface and bulk defects independently from their location. To compute a_{eq}, the flaw fracture origin diameter *d* was measured [39]. The *d* parameter was assessed as reported in Fig. 6a–b, and listed in Table 2. In Table 2, the defect elongation is expressed as D_{Fmax} / D_{Fmin}, showing that the most defects were rather elongated.

The Feret diameter distribution is plotted in Fig. 8a. It is clear that the defects analyzed for room and high temperature samples had slightly different mean values but overlapped when considering the standard deviation. No trend was observed for the defect elongation (D_{Fmax} / D_{Fmin}) and Feret maximum diameter. In Fig. 8b it is depicted how the defect location changed with temperature. For the room temperature tests, only near-surface defects were detected, while for high temperature tests the majority of defects (59 %) were found in the bulk. It is relevant to notice that even if there was undoubtedly a difference in the defect location between room and high temperature tests, this did not cause a measurable change in the Weibull parameter

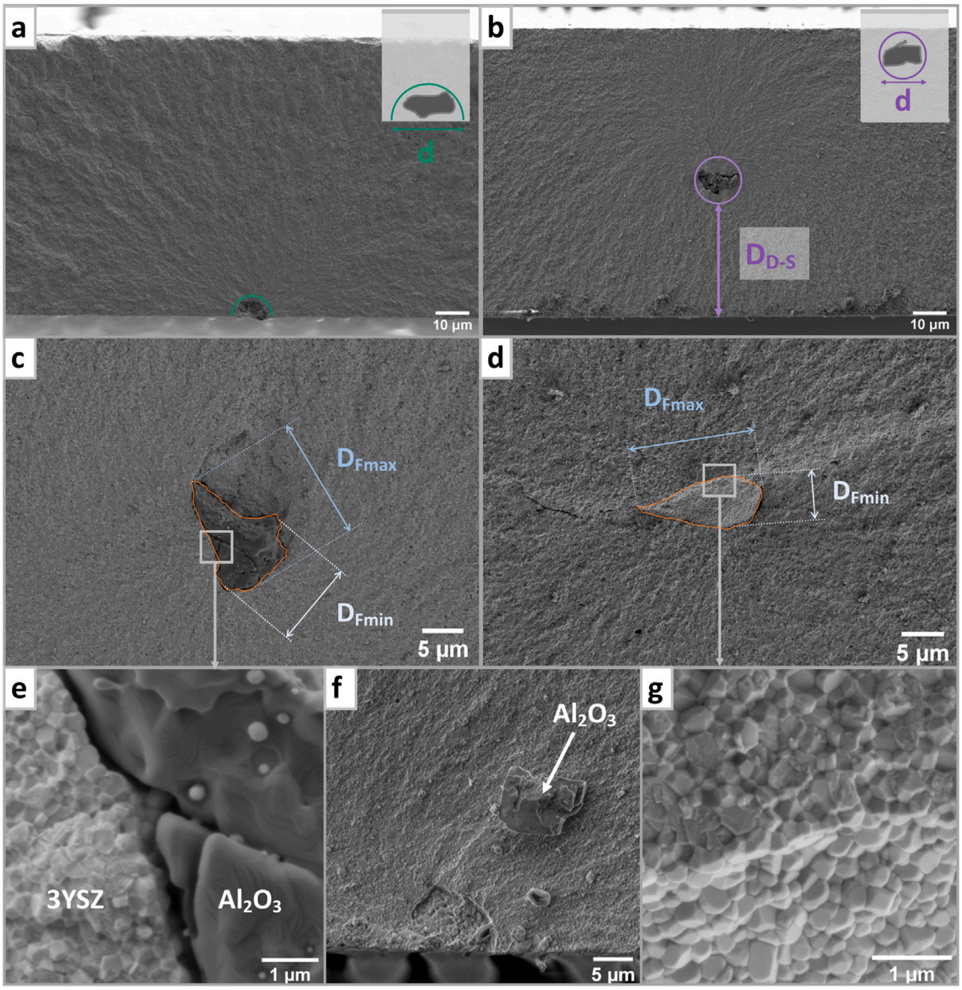

Fig. 6. SEM fractographic analysis details: (a) room-temperature sample with near-surface defect (inclusion): the schematics on the right top shows how the defect diameter was measured [39]; (b) high-temperature sample with bulk defect (inclusion) where the defect diameter is indicated according to the scheme on the top right corner [39], while $D_{D\text{-}S}$ is the distance between the defect and the sample surface; (c) and (d) magnification of, respectively, a bulk inclusion defect and a pore defect (both high-temperature samples): the orange line as the delineation of the defect perimeter and the Feret maximum and minimum diameter are indicated; (e) magnification of c. At the border between 3YSZ and the inclusion: the particle was identified as Al_2O_3 (EDX), and the clearer spots on it was molten Al_2O_3 portions; (f) inclusion defect which was detached from its original position (g) enlargement of picture d. Only unbroken grains are visible on the porosity surface, whereas both intact and cleaved grains are visible on the fracture surface. This indicates a mixed fracture micromechanism, including both trans-granular and inter-granular propagation.

Table 2
Fractographical analysis summary for room and high temperature. The maximum and minimum Feret diameters (D_{Fmax}, D_{Fmin}), together with the defect area were measured as described in Fig. 6. The crack diameter d was measured as illustrated in Fig. 2. The values are expressed as mean and standard deviation.

	Samples (n)	Bulk defects (n)	Near-surface defects [a] (n)	D_{Fmax} (µm)	D_{Fmin} (µm)	D_{Fmax} / D_{Fmin}	A (µm^2)	Diameter of flaw d (µm)
T = 25 °C	27	0	27	10.7 ± 4.3	5.7 ± 2.6	2.2 ± 1.6	44.4 ± 40.1	23.4 ± 6.7
T = 850 °C	24	14	10	13.8 ± 3.1	6.4 ± 1.6	2.2 ± 0.6	57.5 ± 15.2	15.2 ± 3.3

[a] Where the defect to sample surface distance $D_{D\text{-}S}$ (depicted in Fig. 2) is less than D_{Fmax} [38].

m which is a statistical expression of the flaw size and frequency [59]. It is reasonable that the defect location could cause a difference in the *m* parameter if a larger amount of samples would be tested.

Assuming that the defect population was identical for all samples, which is surely true as they were coming from the same exact batch, it is challenging to explain the defect location difference between room and high temperature tests. Excluding the hypothesis that the results were not representative, which is very unlikely for a minimum of 24 samples analyzed, several factors could have contributed to the difference. The first factor is the 3YSZ variation of phase composition between room and high temperature. The tetragonal to monoclinic stress induced phase transformation is absent at high temperature but relevant at room temperature. The toughening mechanism of 3YSZ has different features at the surface compared to the bulk materials. For the room temperature stress-induced tetragonal to monoclinic transformation, not only the local stress level is relevant, but also the grain orientation. Thus, the transformation is more likely to happen at the surface [62]. The sample surface was therefore subjected to transformation at lower stresses making the surface defects more critical than the bulk ones. The high temperature tests were, on the contrary, not affected from the toughening transformation, as the tetragonal phase is stable at T = 850 °C. Therefore the finding of defects also in the bulk. The second factor which could have led to a difference in defect distribution is the fracture micromechanism. As observed in Fig. 7, the fracture micromechanism differs with temperature, which could lead in a different crack development and, consequently, to a

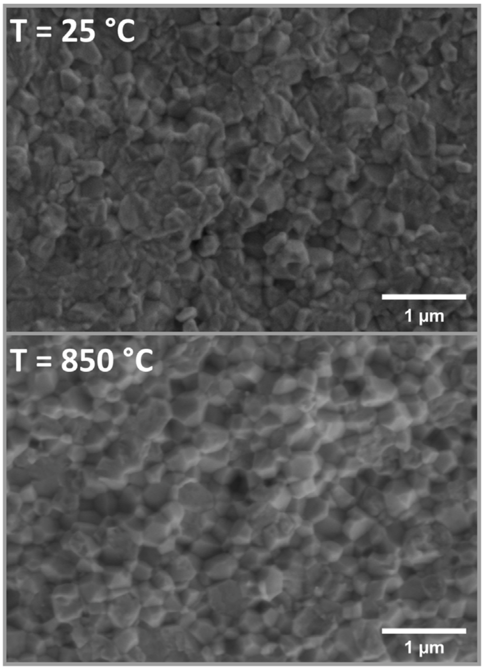

Fig. 7. SEM pictures of two fracture surfaces at high magnification. In both cases (room and high temperature) a mixed fracture micromechanism was observed, as both cleaved grains and entire ones are present. For the room temperature test, the amount of cleaved grains is higher than for the high temperature test.

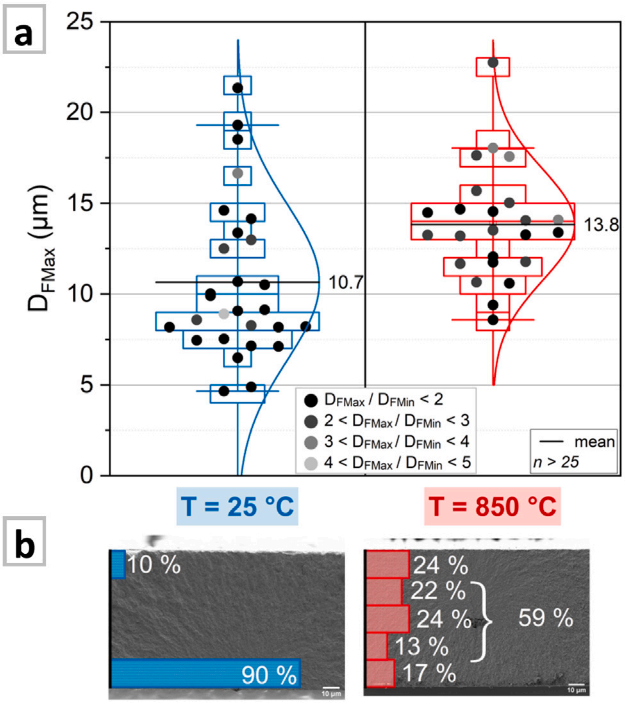

Fig. 8. (a) Maximum Feret diameter for room and high temperature tests, which indicates the defect elongation in terms of D_{Fmax} / D_{Fmin}; (b) location of defects in the sample fracture surface for room and high temperature. Near-surface defects were the only type of defects observed for room temperature tests, while they represent 41 % of the defects for the high temperature tests.

higher relevance of the bulk defects at high temperature. Another possible reason for the difference of crack starting point location was the sample geometry, as the eventual misalignment was perhaps less critical for longer samples [63]. The overall length was higher in the high temperature sample (Fig. 1) which could lead to less critical stress concentrations at the surface. In our previous work [32], the crack initiation was reported at the sample edge, which was in contrast with the results of this work. However, the amount of samples for which the fractographic analysis was performed was confined to four samples with qualitative description aims. On the contrary, the present work data presents a much higher reliableness because of the number of samples analyzed.

In order to correlate the defect size with the tensile strength, the defect location has to be considered. For this reason, the equivalent defect size was calculated [39,40]. For near-surface defects, the equivalent defect size is defined as a_{eq} = 0.25 d, and for bulk defects as a_{eq} = 0.2 d, as illustrated in Fig. 6a–b and in Fig. 9. For ceramics containing flaws, the defects have to be large enough to cause the immediate material fracture without sub-critical crack growth. These materials follow linear elastic fracture mechanics (LEFM, third generation materials [39]), where the local stress intensity factor (K_I) equals the critical stress intensity factor (K_{Ic}). The smaller the defects, the more relevant the material itself in terms of grain size, as the first stage of crack development includes sub-critical crack growth. Determining for the crack development is the comparison between the flaw equivalent size a_{eq} and the grain size. The average grain size of the tested material was $\phi = 246 \pm 94$ nm. The LEFM criterion is valid if $a_{eq} > 150\ \phi$ [39], which was not true in this case. According to this criterion, the defects analyzed were sub-critical, which means that the defects were the starting points for the fracture, but the actual sample failure occurred subsequently to a sub-critical crack developing. For sub-critical defects, the local stress intensity factor (K_I) is not equal to the critical stress intensity factor (K_{Ic}) at the crack starting point. Sub-critical crack growth is not uncommon for many type of ceramics [59], and in this case it is relevant to mention that even if the defects may seem large, an important role was the material grain size.

To check if the tested material corresponded to the sub-critical interpretation, the strength as a function of the equivalent crack length a_{eq} was reported in Fig. 9, where the values of K_{Ic} at room and high temperature are reported [25,54]. Almost all the data points for room and high temperature were located in proximity or on the left part of the K_{Ic} line. For both temperature data, it can be seen how the smaller defects deviated from the K_{Ic} line and tended to a direction which was parallel to the x-axis. The theoretical parallel line to the x-axis would be the region where flaws are so small that they are irrelevant for the final strength and the only contribution is attributed to the material grain size. This type of materials is classified as first generation [39]. For larger defects a_{eq} > 4 µm, the room and high temperature data points were located in the LEFM region, in proximity of the K_{Ic} line. The defects smaller than a_{eq} = 4 µm were rather separating from the K_{Ic} line. This observation allows the assumption that from defects bigger a_{eq} = 4 µm the material follows the LEFM theory where the local stress intensity factor equals the critical stress intensity factor ($K_I = K_{Ic}$) and the defects are considered critical. In this condition, the sub-critical crack growth had a negligible effect and the main contribution to the strength was provided by the defect size. For a_{eq} < 4 µm, instead, the strength was determined by a combination of the defect size and the grain size. Sub-critical crack growth occurred close to the bigger defects in the beginning ($K_I \neq K_{Ic}$). In the following stage, the crack expanded in the material depending on the grain size, up until the sample failure as the defect reached the critical size. The observed behavior is largely known and was reported in the literature for various ceramic materials [64], however the correlation between defect size and strength for 3YSZ thin tapes was determined for the first time in the present work. These findings are relevant to set a limit for allowable defect sizes in 3YSZ tapes with similar grain size ($\phi = 246 \pm 94$ nm). The material analyzed was therefore not following the LEFM theory from $\frac{a_{eq}}{\phi} = \frac{4}{0.246} = 16$. The found value restricts the limit previously set in the literature [39] describing more precisely the specific material

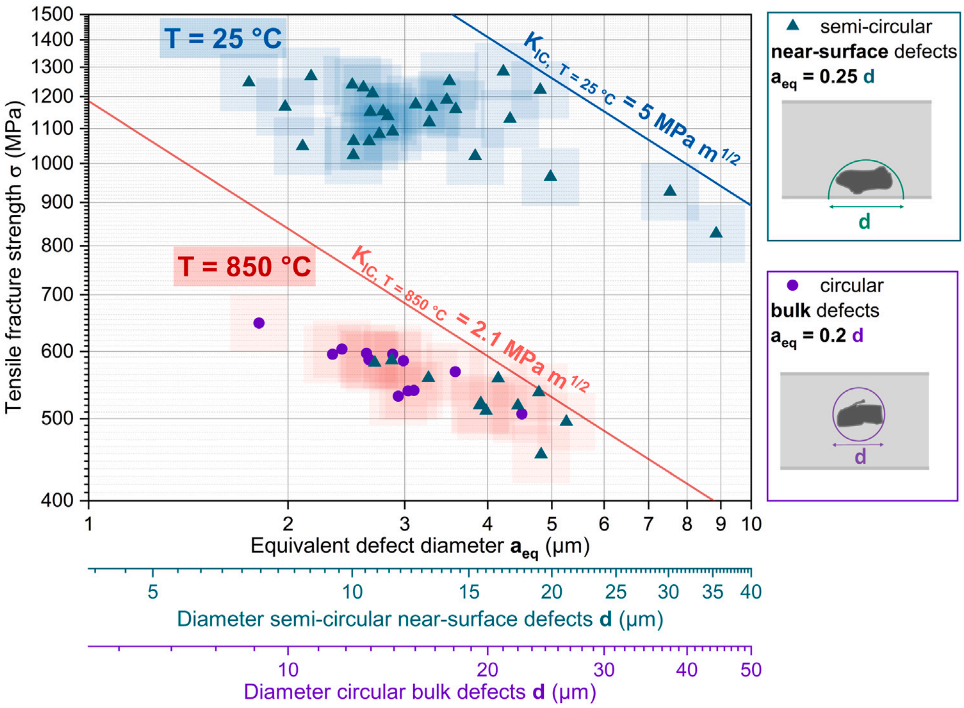

Fig. 9. Fracture strength as a function of equivalent crack size for room temperature and T = 850 °C in logarithmic scale, on the x-axis the corresponding flaw diameter calculated as from the right scheme. The K_{Ic} values are reported from the literature [25,54].

analyzed. Fig. 9 shows that the equivalent crack length of a_{eq} = 4 µm corresponds to a diameter of $d_{near\text{-}surface}$ = 16 µm for near-surface semi-circular defects and a diameter of d_{bulk} = 20 µm for bulk circular defects. For smaller defect diameters, the strength measured was never below σ_{RT} = 1000 MPa for room temperature and $\sigma_{850\ °C}$ = 500 MPa for high temperature. In Fig. 9 it can be noticed that for the high temperature tests the defects corresponding to lower strength values were near-surface ones. This remark indicates the importance of surface defects more than bulk defects not only at room temperature but also at operating temperature.

3.3. In-situ nanoindentation

To evaluate the local mechanical properties of the 3YSZ electrolyte, in-situ nanoindentation was additionally performed at room and high temperature and the results are summarized in Table 3. After the tests, SEM recordings of the indents were carried out and are shown in Fig. 10. The projected contact area and indentation depth values increased with a higher temperature. The SEM indents area showed an equally increment of projected contact area, which supported the validity of the nanoindentation measurements. The room temperature hardness was comparable with the literature data of similar materials [65–67]. At T = 650 °C, the hardness decreased by 62 % compared to room temperature. Even if high temperature indentation was not yet performed on 3YSZ dense electrolytes, a decrease in indentation hardness by temperature increase was previously observed on porous zirconia coatings [68], and single crystals [69]. The Young's modulus measured at high temperature had a high standard deviation, indicating a lower measurement precision. However, the value measured is compatible with the one determined with the tensile testing at higher temperature (Table 1). At T = 250 °C, The Young's modulus decreased, then increased again until T = 650 °C. The local Young's modulus of cubic zirconia was previously measured with nanoindentation [70] showing a decrease from room temperature to T = 300 °C and then a stabilization until T = 500 °C. An increase of Young's modulus was reported with the utilization of the micro indentation technique between room temperature and T = 500 °C [71]. The high temperature Young's moduli measured in this work by nanoindentation are not matching the impulse excitation technique (IET) data on 3YSZ tapes [54], which is not a local measurement technique. The discrepancies of hardness and Young's modulus between the different methods show the challenges which characterize these measurements, especially at high temperature. Nevertheless, an increase in plasticity by temperature increase was proved by the reduction of hardness and Young's modulus. The finding was confirmed by the visual examination of the indent imprints after the test as shown in Fig. 10. In the surface indented at room temperature the blurred grain boundaries are clearly visible, as reported in the literature [67]. At higher temperatures, the grain boundaries start become less noticeable indicating an increase of plastic behavior.

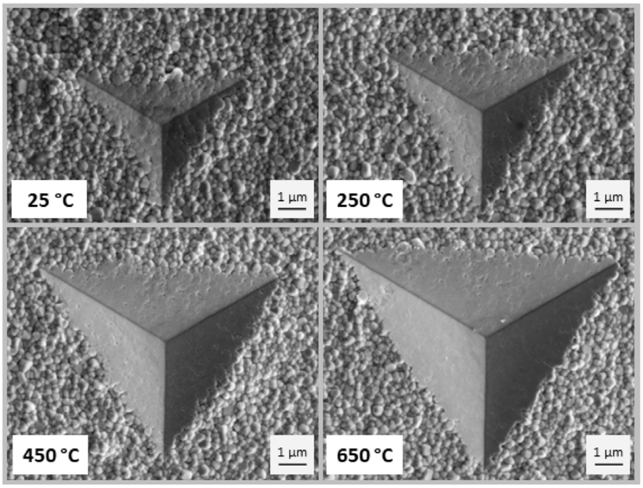

Fig. 10. SEM images of representative indents after the test at different temperatures with maximum load of 250 mN.

Table 3

Nanoindentation test results in terms of hardness, Young's modulus, projected contact area and maximum indentation depth at room and high temperature. The values are expressed as mean and standard deviation.

Temperature (°C)	Hardness[a] (GPa)	Young's modulus[a] (GPa)	Projected contact area[b] (μm^2)	Indentation depth[b] (μm)
25	16.3 ± 2.1	230 ± 48	16 ± 2	0.94 ± 0.07
250	10.2 ± 0.9	166 ± 13	25 ± 2	1.16 ± 0.04
450	7.5 ± 0.5	175 ± 8	35 ± 2	1.29 ± 0.03
650	6.2 ± 0.3	196 ± 13	42 ± 2	1.40 ± 0.02

[a] Average of 10 cyclic loading indentation tests from 20 to 250 mN.

[b] Calculated on the maximum load of F = 250 mN.

4. Summary and outlook

The tensile strength of 3YSZ ultrathin (t = 90 μm) tapes for solid oxide cells was evaluated at room and operating temperature (T = 850 °C), showing a 50 % lower strength at T = 850 °C compared to room temperature. The 90 % (n = 27/30) test validity confirmed the test reliableness at high temperature. The characteristic strength and Weibull modulus were measured, resulting in $\sigma_{0,RT}$ = 1174 MPa, m_{RT} = 13.6, $\sigma_{0,850\,°C}$ = 576 MPa and $m_{850\,°C}$ = 14.8. The effective evaluated volume was V_{eff} = 4.1 μm^3, which was 330 times smaller than the estimated electrolyte volume in the cell. However, the test owns a better reliability than the bending tests where the stress is surface-concentrated and not representative of the material's bulk. An estimation of the strength for the complete electrolyte size was computed based on these values and the Weibull theory. As a result, for an electrolyte 100 × 150 mm large and with a thickness of t = 90 μm, the strength was estimated as $\sigma_{0,\,RT} \approx 700$ MPa and $\sigma_{0,\,850\,°C} \approx 370$ MPa.

A fractographic analysis was performed for each of the valid samples and the defects observed included particle inclusions as well as large pores and regions with agglomerated small porosity. The defects were mainly located at the sample surface for the room temperature tests and at the sample surface or in bulk for the high temperature tests. This difference was attributed to several factors including the stress induced toughening mechanism and the fracture micromechanism. To measure the defects, the maximum Feret diameter was determined: $D_{Fmax,\,RT}$ = 10.7 ± 4.3 μm and $D_{Fmax,\,850\,°C}$ = 13.8 ± 3.1 μm. The strength at room and high temperature as a function of the defect size was plotted. It was observed that the material analyzed deviated from the linear elastic fracture mechanics (LEFM) for smaller defects. The surface defects with diameter $d_{near\text{-}surface} > 16$ μm, or the bulk defect with diameter $d_{bulk} > 20$ μm were evaluated as critical, which means their size was the main factor influencing the sample strength. The strength of the samples with smaller defects deviated from the linear elastic fracture mechanics (LEFM) theory. These were evaluated as sub-critical and sub-critical crack growth was assumed to occur before the sample failure. For the sub-critical defects, the strength depended not only on the local stresses but also on the material grain size distribution.

In-situ nanoindentation was performed on the 3YSZ tapes to determine the local mechanical properties at high temperature for the first time. At the maximum temperature reported, T = 650 °C, the hardness and the Young's modulus showed a decrease of 62 % and 15 % respectively compared to room temperature. The high standard deviation in the Young's modulus and the discrepancies between different methods from the literature denoted the challenges in investigating the local mechanical properties of these materials, especially at high temperature. Yet, the increase of plasticity by increasing temperature was observed with the nanoindentation test and was also proved by the SEM examination of the indents after the test.

The results presented are a significant step forward in understanding the failure mechanisms of 3YSZ tapes for SOCs operating at high temperature. The evidence of different types of defects on the fracture surface raise the questions of how high their density is in the specimens and to what extent are the electrochemical properties affected from it. The demonstrated presence of sub-critical crack growth brings up the possibility that this phenomenon may play a role in the long-term stability of the 3YSZ electrolyte during the cell operation.

CRediT authorship contribution statement

Ilaria Bombarda: Writing – review & editing, Writing – original draft, Visualization, Validation, Methodology, Investigation, Formal analysis, Data curation, Conceptualization. **Felix Wich:** Validation, Methodology, Investigation. **Nico Langhof:** Writing – review & editing, Supervision, Resources, Project administration, Funding acquisition, Conceptualization. **Carolin Sitzmann:** Writing – review & editing, Supervision, Resources, Project administration, Funding acquisition, Conceptualization. **Stefan Schafföner:** Writing – review & editing, Supervision, Resources, Project administration, Funding acquisition, Conceptualization.

Declaration of competing interest

The authors declare that they have no known competing financial interests or personal relationships that could have appeared to influence the work reported in this paper.

Acknowledgments

We gratefully acknowledge financial support from the German Ministry of Education and Research (BMBF) within the framework of the project H_2-Giga, subproject HTEL-Stacks, via the grant number 03HY124D. We acknowledge the German Research Foundation (DFG) for providing the ZwickRoell universal testing machine, grant number: 428091604. We acknowledge Kerafol Keramische Folien GmbH and Sunfire GmbH for the collaboration and for providing the materials. Bernd Martin from the University of Bayreuth is acknowledged for the technical support for the testing setup and gluing device design. Norbert Löffler and Frank Neumann from the University of Bayreuth are acknowledged for the sample grinding.

Appendix A. Supplementary data

Supplementary material related to this article can be found online at https://doi.org/10.1016/j.ijhydene.2025.150764.

References

[1] Liu H, Yu M, Tong X, Wang Q, Chen M. High temperature solid oxide electrolysis for green hydrogen production. Chem Rev 2024;124(18):10509–76. http://dx.doi.org/10.1021/acs.chemrev.3c00795.

[2] Prosser JH, James BD, Murphy BM, Wendt DS, Casteel MJ, Westover TL, et al. Cost analysis of hydrogen production by high-temperature solid oxide electrolysis. Int J Hydrog Energy 2024;49:207–27. http://dx.doi.org/10.1016/j.ijhydene.2023.07.084.

[3] Eikeng E, Makhsoos A, Pollet BG. Critical and strategic raw materials for electrolysers, fuel cells, metal hydrides and hydrogen separation technologies. Int J Hydrog Energy 2024;71:433–64. http://dx.doi.org/10.1016/j.ijhydene.2024.05.096.

[4] McKinsey & Company. Hydrogen insights 2023: An update on the state of the global hydrogen economy, with a deep dive into North America. 2023, URL https://hydrogencouncil.com/wp-content/uploads/2023/05/Hydrogen-Insights-2023.pdf.

[5] Chatenet M, Pollet BG, Dekel DR, Dionigi F, Deseure J, Millet P, et al. Water electrolysis: from textbook knowledge to the latest scientific strategies and industrial developments. Chem Soc Rev 2022;51:4583–762. http://dx.doi.org/10.1039/d0cs01079k.

[6] Mogensen MB, Chen M, Frandsen HL, Graves C, Hansen JB, Hansen KV, et al. Reversible solid-oxide cells for clean and sustainable energy. Clean Energy 2019;3:175–201. http://dx.doi.org/10.1093/ce/zkz023.

[7] Posdziech O, Schwarze K, Brabandt J. Efficient hydrogen production for industry and electricity storage via high-temperature electrolysis. Int J Hydrog Energy 2019;44(35):19089–101. http://dx.doi.org/10.1016/j.ijhydene.2018.05.169.

[8] Nami H, Rizvandi OB, Chatzichristodoulou C, Hendriksen PV, Frandsen HL. Techno-economic analysis of current and emerging electrolysis technologies for green hydrogen production. Energy Convers Manag 2022;269:116162. http://dx.doi.org/10.1016/j.enconman.2022.116162.

[9] Lange H, Klose A, Lippmann W, Urbas L. Technical evaluation of the flexibility of water electrolysis systems to increase energy flexibility: A review. Int J Hydrog Energy 2023;48(42):15771–83. http://dx.doi.org/10.1016/j.ijhydene.2023.01.044.

[10] Hussain S, Yangping L. Review of solid oxide fuel cell materials: cathode, anode, and electrolyte. Energy Trans 2020;4:113–26. http://dx.doi.org/10.1007/s41825-020-00029-8.

[11] Kaur G. Solid oxide fuel cell components. Springer International Publishing; 2016, http://dx.doi.org/10.1007/978-3-319-25598-9.

[12] Riegraf M, Amaya-Dueñas DM, Sata N, Friedrich KA, Costa R. Performance and limitations of nickel-doped chromite anodes in electrolyte-supported solid oxide fuel cells. ChemSusChem 2021;14(11):2401–13. http://dx.doi.org/10.1002/cssc.202100330.

[13] Masini A, Strohbach T, Šiška F, Chlup Z, Dlouhý I. Electrolyte-supported fuel cell: Co-sintering effects of layer deposition on biaxial strength. Materials 2019;12. http://dx.doi.org/10.3390/ma12020306.

[14] Börger A, Supancic P, Danzer R. The ball on three balls test for strength testing of brittle discs: stress distribution in the disc. J Eur Ceram Soc 2002;22:1425–36. http://dx.doi.org/10.1016/S0955-2219(01)00458-7.

[15] Börger A, Supancic P, Danzer R. The ball on three balls test for strength testing of brittle discs: Part II: analysis of possible errors in the strength determination. J Eur Ceram Soc 2004;24:2917–28. http://dx.doi.org/10.1016/j.jeurceramsoc.2003.10.035.

[16] Danzer R, Supancic P, Herrer W. Biaxial tensile strength test for brittle rectangular plates. J Ceram Soc Jpn 2006;114(11):1054–60. http://dx.doi.org/10.2109/jcersj.114.1054.

[17] Faes A, Frandsen HL, Kaiser A, Pihlatie M. Strength of anode-supported solid oxide fuel cells. Fuel Cells 2011;11(5):682–9. http://dx.doi.org/10.1002/fuce.201100038.

[18] Bermejo R, Supancic P, Aldrian F, Danzer R. Experimental approach to assess the effect of metallization on the strength of functional ceramic components. Scr Mater 2012;66(8):546–9. http://dx.doi.org/10.1016/j.scriptamat.2011.12.029.

[19] Fleischhauer F, Terner M, Bermejo R, Danzer R, Mai A, Graule T, et al. Fracture toughness and strength distribution at room temperature of zirconia tapes used for electrolyte supported solid oxide fuel cells. J Power Sources 2015;275:217–26. http://dx.doi.org/10.1016/j.jpowsour.2014.10.083.

[20] Masini A, Šiška F, Ševeček O, Chlup Z, Dlouhy I. Elastic properties of multi-layered ceramic systems for SOCs. Int J Appl Ceram Technol 2018;15:370–9. http://dx.doi.org/10.1111/ijac.12801.

[21] Pećanac G, Bause T, Malzbender J. Ring-on-ring testing of thin, curved bi-layered materials. J Eur Ceram Soc 2011;31:2037–42. http://dx.doi.org/10.1016/j.jeurceramsoc.2011.05.021.

[22] Morrell R. Biaxial flexural strength testing of ceramic materials - Measurement good practice guide no. 12. UK: National Physical Laboratory; 1998

[23] Hsueh CH, Luttrell C, Becher PF. Analyses of multilayered dental ceramics subjected to biaxial flexure tests. Dent Mater 2006;22:460–9. http://dx.doi.org/10.1016/j.dental.2005.04.037.

[24] Malzbender J, Steinbrech RW. Fracture test of thin sheet electrolytes for solid oxide fuel cells. J Eur Ceram Soc 2007;27:2597–603. http://dx.doi.org/10.1016/j.jeurceramsoc.2006.11.071.

[25] Kuebler J, Vogt UF, Haberstock D, Sfeir J, Mai A, Hocker T, et al. Simulation and validation of thermo-mechanical stresses in planar SOFCs. Fuel Cells 2010;10(6):1066–73. http://dx.doi.org/10.1002/fuce.201000040.

[26] Hsueh CH, Lance MJ, Ferber MK. Stress distributions in thin bilayer discs subjected to ball-on-ring tests. J Am Ceram Soc 2005;88(6):1687–90. http://dx.doi.org/10.1111/j.1551-2916.2005.00343.x.

[27] Fett T, Rizzi G, Ernst E, Müller R, Oberacker R. A 3-balls-on-3-balls strength test for ceramic disks. J Eur Ceram Soc 2007;27:1–12. http://dx.doi.org/10.1016/j.jeurceramsoc.2006.02.033.

[28] Faes A, Lund-Frandsen H, Pihlatie M, Kaiser A, Goldstein DR. Curvature and strength of Ni-YSZ solid oxide half-cells after redox treatments. J Eng Mater Technol Trans ASME 2010;7(5):237–45. http://dx.doi.org/10.1115/1.4001019.

[29] Porporati AA, Miyatake T, Schilcher K, Zhu W, Pezzotti G. Ball-on-ring test in ceramic materials revisited by means of fluorescence piezospectroscopy. J Eur Ceram Soc 2011;31:2031–6. http://dx.doi.org/10.1016/j.jeurceramsoc.2011.05.009.

[30] Lupercio AE, Moshkelgosha E, Winters RC, Doyle C, Mamivand M, Nelson AT, et al. Ball–on–ring test validation for equibiaxial flexural strength testing of engineered ceramics. Int J Ceram Eng Sci 2021;3:128–39. http://dx.doi.org/10.1002/ces2.10085.

[31] Riegraf M, Bombarda I, Dömling F, Liensdorf T, Sitzmann C, Langhof N, et al. Enhancing the mechanical strength of electrolyte-supported solid oxide cells with thin and dense doped-ceria interlayers. ACS Appl Mater Interfaces 2021;13(42):49879–89. http://dx.doi.org/10.1021/acsami.1c13899.

[32] Bombarda I, Sitzmann C, Liensdorf T, Langhof N, Schafföner S. Tensile testing of yttria-stabilized zirconia ceramic tapes for solid oxide cells. Int J Hydrog Energy 2024;50:492–500. http://dx.doi.org/10.1016/j.ijhydene.2023.08.258.

[33] Danzer R. On the relationship between ceramic strength and the requirements for mechanical design. J Eur Ceram Soc 2014;34:3435–60. http://dx.doi.org/10.1016/j.jeurceramsoc.2014.04.026.

[34] Freimann S, Meckolsky J. The fracture of brittle materials, vol. 18, USA: The American Ceramic Society; 1967.

[35] Bradt RC, Hasselman DPH, Munz D, Sakai M, Shevchenko V. Fracture mechanics of ceramics: Volume 10 fracture fundamentals, high-temperature deformation, damage, and design. USA: Springer Science+Business Media New York; 1992, http://dx.doi.org/10.1007/978-1-4615-3348-1.

[36] Danzer R. Some notes on the correlation between fracture and defect statistics: Are Weibull statistics valid for very small specimens? J Eur Ceram Soc 2006;26(15):3043–9. http://dx.doi.org/10.1016/j.jeurceramsoc.2005.08.021.

[37] Lei W-S, Zhang P, Yu Z, Qian G. Statistics of ceramic strength: Use ordinary Weibull distribution function or Weibull statistical fracture theory? Ceram Int 2020;46(13):20751–68. http://dx.doi.org/10.1016/j.ceramint.2020.05.024.

[38] Quinn GD. NIST recommended practice guide fractography of ceramics and glasses. National Institute of Standards and Technology; 2016, http://dx.doi.org/10.6028/NIST.SP.960-16e2.

[39] Usami S, Kimoto H, Takahashi I, Shida S. Strength of ceramic materials containing small flaws. Eng Fract Mech 1986;4(23):745–61. http://dx.doi.org/10.1016/0013-7944(86)90120-7.

[40] Matsuda S. Fracture characteristics of silicon nitride ceramic ball subjected to thermal shock. J Mater Sci 2016;51(11):5502–13. http://dx.doi.org/10.1007/s10853-016-9855-1.

[41] Hoshide T, Hiramatsu H. Characterization of integrated data on inherent flaws in engineering ceramics. Mater Sci Res Int 1999;(5):285–90. http://dx.doi.org/10.2472/jsms.48.12Appendix_285.

[42] Moon H, Kim S, Hyun S, Kim H. Development of IT-SOFC unit cells with anode-supported thin electrolytes via tape casting and co-firing. Int J Hydrog Energy 2008;33(6):1758–68. http://dx.doi.org/10.1016/j.ijhydene.2007.12.062.

[43] ASM International. C1273 – 18 standard test method fortensile strength of monolithic advanced ceramics at ambient temperatures, vol. i, USA: ASTM International; 2018, http://dx.doi.org/10.1520/C1273-18.

[44] Klemensø T, Lund E, Sørensen BF. Optimal shape of thin tensile test specimen. J Am Ceram Soc 2007;90(6):1827–35. http://dx.doi.org/10.1111/j.1551-2916.2007.01538.x.

[45] Celik S, Timurkutluk B, Toros S, Timurkutluk C. Mechanical and electrochemical behavior of novel electrolytes based on partially stabilized zirconia for solid oxide fuel cells. Ceram Int 2015;41(7):8785–90. http://dx.doi.org/10.1016/j.ceramint.2015.03.104.

[46] Flauder S, Bombarda I, D'Ambrosio R, Langhof N, Lazzeri A, Krenkel W, et al. Size effect of carbon fiber-reinforced silicon carbide composites (C/C-SiC): Part 2 - tensile testing with alignment device. J Eur Ceram Soc 2022;42(4):1227–37. http://dx.doi.org/10.1016/j.jeurceramsoc.2021.11.044.

[47] Flauder S, Langhof N, Schafföner S. The role of alignment for valid tensile testing of ceramic matrix composites. J Eur Ceram Soc 2025;45(3):117001. http://dx.doi.org/10.1016/j.jeurceramsoc.2024.117001.

[48] Taskonak B, Yan J, Mecholsky JJ. Fracture surface analysis of dental ceramics. Ceram Trans 2007;199:271–9. http://dx.doi.org/10.1002/9781118144152.ch21.

[49] ASTM. C1322 – 05b sandard practice for fractography and characterization of fracture origins in advanced ceramics. West Conshohocken, PA: ASTM International; 2010, http://dx.doi.org/10.1520/C1322-05BR10.

[50] Merkus HG. Particle size measurements: Fundamentals, Practice, Quality. New York, NY: Springer; 2009.

[51] DIN EN ISO. 13383-1 Hochleistungskeramik – Mikrostrukturelle Charakterisierung – Teil 1: Bestimmung der Korngröße und der Korngrößenverteilung. 2016, http://dx.doi.org/10.31030/2482451.

[52] ASTM. E112-12 test methods for determining average grain size. West Conshohocken, PA: ASTM International; 2012, http://dx.doi.org/10.1520/E0112-12.

[53] Oliver WC, Pharr GM. Measurement of hardness and elastic modulus by instrumented indentation: Advances in understanding and refinements to methodology. J Mater Res 2004;19:3–20. http://dx.doi.org/10.1557/jmr.2004.19.1.3.

[54] Fleischhauer F, Bermejo R, Danzer R, Mai A, Graule T, Kuebler J. High temperature mechanical properties of zirconia tapes used for electrolyte supported solid oxide fuel cells. J Power Sources 2015;273:237–43. http://dx.doi.org/10.1016/j.jpowsour.2014.09.068.

[55] Matsui M, Soma T, Oda I. Stress–Induced transformation and plastic deformation for Y2O3–containing tetragonal zirconia polycrystals. J Am Ceram Soc 1986;69(3):198–202. http://dx.doi.org/10.1111/j.1151-2916.1986.tb07406.x.

[56] Leoni M, Jones R, Scardi P. Phase stability of scandia–yttria-stabilized zirconia TBCs. Surf Coatings Technol 1998;108–109:107–13. http://dx.doi.org/10.1016/S0257-8972(98)00617-3.

[57] Acala J, Anglada M. High-temperature crack growth in Y-TZP. Mater Sci Eng A 1997;103–9. http://dx.doi.org/10.1016/S0921-5093(97)00106-8.

[58] Liang C, Tong K, Huang J, Bu Y, Liu J, Zhao Z, et al. Extreme dislocation-mediated plasticity of yttria-stabilized zirconia. Mater Today Phys 2022;22:100588. http://dx.doi.org/10.1016/j.mtphys.2021.100588.

[59] Danzer R, Lube T, Supancic P, Damani R. Fracture of ceramics. Adv Eng Mater 2008;10(4):275–98. http://dx.doi.org/10.1002/adem.200700347.

[60] Griffith AA. The phenomena of rupture and flow in solids. Philos Trans R Soc Lond 1920;221:163–98. http://dx.doi.org/10.1098/rsta.1921.0006.

[61] Newman Jr J, Raju I. Stress-intensity factor equations for cracks in three-dimensional finite bodies. 1981, http://dx.doi.org/10.1016/0013-7944(81)90116-8.

[62] Chevalier J, Gremillard L, Virkar AV, Clarke DR. The tetragonal–monoclinic transformation in zirconia: Lessons learned and future trends. J Am Ceram Soc 2009;92(9):1901–20. http://dx.doi.org/10.1111/j.1551-2916.2009.03278.x.

[63] Davis JR. Tensile testing. USA: ASM International; 2004.

[64] Hu X, Mai Y-W. Re-interpretation of the Weibull strength distribution of polycrystalline ceramics – characteristic strength and fracture toughness. J Mech Phys Solids 2025;196:106021. http://dx.doi.org/10.1016/j.jmps.2024.106021.

[65] Ren X, Pan W. Mechanical properties of high-temperature-degraded yttria-stabilized zirconia. Acta Mater 2014;69:397–406. http://dx.doi.org/10.1016/j.actamat.2014.01.017.

[66] Ghatee M, Salihi H. Investigation of the mechanical properties of various yttria stabilized zirconia based thin films prepared by aqueous tape casting. Adv Ceram Prog 2017;(3):26–30. http://dx.doi.org/10.30501/acp.2017.70042.

[67] Kosai K, Yan J. Effects of cyclic loading on subsurface microstructural changes of zirconia polycrystals in nanoscale mechanical processing. Int J Mach Tools Manuf 2020;159:103626. http://dx.doi.org/10.1016/j.ijmachtools.2020.103626.

[68] He R, Qu Z, Pei Y, Fang D. High temperature indentation tests of YSZ coatings in air up to 1200 °C. Mater Lett 2017;209:5–7. http://dx.doi.org/10.1016/j.matlet.2017.07.091.

[69] Morscher GN, Pirouz P, Heuer AH. Temperature dependence of hardness in yttria–stabilized zirconia single crystals. J Am Ceram Soc 1991;74(3):491–500. http://dx.doi.org/10.1111/j.1151-2916.1991.tb04049.x.

[70] Masuda H, Morita K, Ohmura T. Nanoindentation-induced plasticity in cubic zirconia up to 500 °C. Acta Mater 2020;184:59–68. http://dx.doi.org/10.1016/j.actamat.2019.11.028.

[71] Cho J, Li Q, Wang H, Fan Z, Li J, Xue S, et al. High temperature deformability of ductile flash-sintered ceramics via in-situ compression. Nat Commun 2018;9(1):2063. http://dx.doi.org/10.1038/s41467-018-04333-2.